

**Ferromagnetic helical nodal line and Kane-Mele spin-orbit coupling in kagome metal Fe<sub>3</sub>Sn<sub>2</sub>**Shiang Fang<sup>1,\*</sup>, Linda Ye<sup>2,\*</sup>, Madhav Prasad Ghimire<sup>3,4</sup>, Mingu Kang<sup>2,5</sup>, Junwei Liu<sup>6</sup>, Minyong Han<sup>2</sup>, Liang Fu<sup>2</sup>, Manuel Richter<sup>4,7</sup>, Jeroen van den Brink<sup>4,8</sup>, Efthimios Kaxiras<sup>9,10</sup>, Riccardo Comin<sup>2</sup>, and Joseph G. Checkelsky<sup>2,§</sup><sup>1</sup>*Department of Physics and Astronomy, Center for Materials Theory, Rutgers University, Piscataway, New Jersey 08854, USA*<sup>2</sup>*Department of Physics, Massachusetts Institute of Technology, Cambridge, Massachusetts 02139, USA*<sup>3</sup>*Central Department of Physics, Tribhuvan University, Kirtipur, 44613, Kathmandu, Nepal*<sup>4</sup>*Leibniz Institute for Solid State and Materials Research, IFW Dresden, Helmholtzstraße 20, 01069 Dresden, Germany*<sup>5</sup>*Max Planck POSTECH Korea Research Initiative, Center for Complex Phase of Materials, Pohang 37673, Republic of Korea*<sup>6</sup>*Department of Physics, Hong Kong University of Science and Technology, Clear Water Bay, Hong Kong, China*<sup>7</sup>*Dresden Center for Computational Materials Science (DCMS), TU Dresden, 01062 Dresden, Germany*<sup>8</sup>*Würzburg-Dresden Cluster of Excellence ct.qmat, Technische Universität Dresden, 01062 Dresden, Germany*<sup>9</sup>*Department of Physics, Harvard University, Cambridge, Massachusetts 02138, USA*<sup>10</sup>*John A. Paulson School of Engineering and Applied Sciences, Harvard University, Cambridge, Massachusetts 02138, USA*

(Received 29 March 2021; accepted 24 November 2021; published 5 January 2022)

The two-dimensional kagome lattice hosts Dirac fermions at its Brillouin zone corners  $K$  and  $K'$ , analogous to the honeycomb lattice. In the density functional theory electronic structure of ferromagnetic kagome metal Fe<sub>3</sub>Sn<sub>2</sub>, without spin-orbit coupling, we identify two energetically split helical nodal lines winding along  $z$  in the vicinity of  $K$  and  $K'$  resulting from the trigonal stacking of the kagome layers. We find that hopping across A-A stacking introduces a layer splitting in energy while that across A-B stacking controls the momentum space amplitude of the helical nodal lines. We identify the latter to be one order of magnitude weaker than the former owing to the underlying  $d$ -orbital degrees of freedom. The effect of spin-orbit coupling is found to resemble that of a Kane-Mele term, where the nodal lines can either be fully gapped to quasi-two-dimensional massive Dirac fermions, or remain gapless at discrete Weyl points depending on the ferromagnetic moment orientation. Aside from numerically establishing Fe<sub>3</sub>Sn<sub>2</sub> as a model Dirac kagome metal by clarifying the roles played by interplane coupling, our results provide insights into materials design of topological phases from the lattice point of view, where paradigmatic low dimensional lattice models often find realizations in crystalline materials with three-dimensional stacking.

DOI: [10.1103/PhysRevB.105.035107](https://doi.org/10.1103/PhysRevB.105.035107)**I. INTRODUCTION**

Topological nodal lines are one-dimensional manifolds of band degeneracies in momentum space first introduced conceptually by Burkov *et al.* in 2011 as a higher dimensional generalization of pointlike band touching [1]. Such line nodes have in recent years found realizations in various forms in crystalline materials, including infinite lines extending over Brillouin zones [2], closed loops [3], along with intricate three-dimensional networks of chains, knots, and nexuses [4–9]. Interest in electronic line nodes are partly motivated by the peculiar emergent condensed matter quasiparticles they support, which do not possess fundamental particle analogues [4]. Furthermore, due to bulk-boundary correspondence, nodal lines in three-dimensional bulk materials generate surface states enclosed in their surface projection; these signature surface states under certain circumstances

bear little momentum-space dispersion over a finite region in the surface Brillouin zone [1] and are therefore termed “drumhead surface states.” The enhanced density of states of drumhead surface states is expected to provide a route towards high-temperature correlated phases including ferromagnetism and superconductivity [10].

Viewed in the context of band topology, nodal lines in three-dimensional materials are necessarily protected by symmetries [8] and therefore serve as progenitors for a large number of distinct topological electronic states when the corresponding symmetry is relieved. For instance, broken mirror symmetry is suggested to separate intersecting nodal lines and serve to manipulate an embedded non-Abelian topology [7]. The prototype inversion symmetry-breaking Weyl semimetal TaAs [11] and time-reversal symmetry breaking Weyl semimetal Co<sub>3</sub>Sn<sub>2</sub>S<sub>2</sub> [12] can both be viewed as generated by adding spin-orbit coupling—which breaks the SU(2) spin-rotation symmetry—to nodal loops on mirror planes. In addition, nodal lines in certain cases can be fully gapped and further give rise to topological insulating phases [9]. From the materials perspective, elucidating mechanisms of generating topological nodal lines and their interplay with different types of symmetries—including crystallographic symmetries, spin-rotation symmetry, and time-reversal symmetry—are expected to afford key clues in discovering novel topological

\*These authors contributed equally to this work.

†Present address: Department of Physics, Massachusetts Institute of Technology, Cambridge, Massachusetts 02139, USA.

‡Present Address: Department of Applied Physics, Stanford University, Stanford, California 94305, USA.

§checkelsky@mit.edu

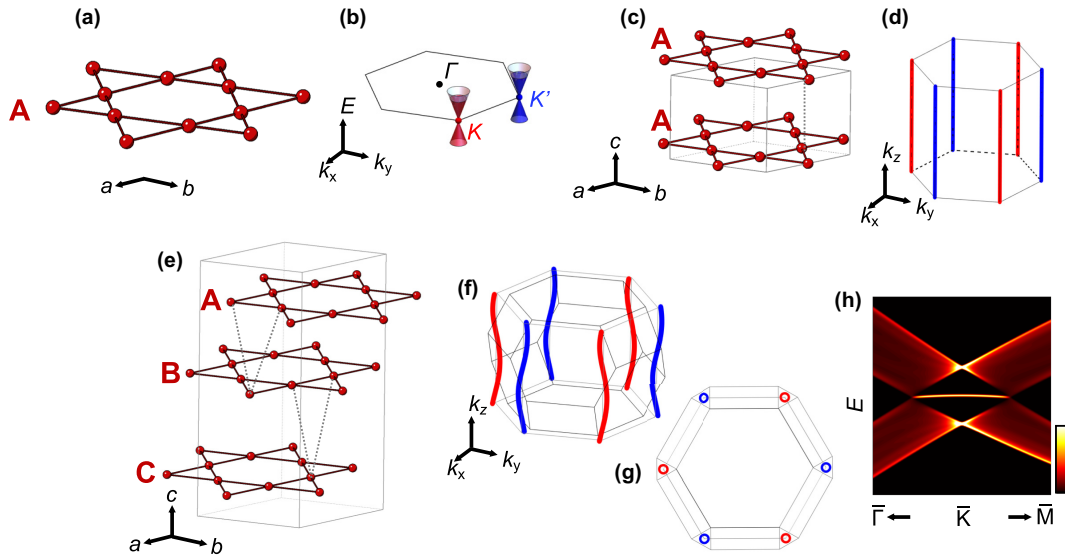


FIG. 1. Nodal lines and three-dimensional stacking of the kagome lattice. (a) The two-dimensional (2D) kagome lattice and (b) associated Dirac fermions in the hexagonal Brillouin zone (BZ). Blue and red Dirac fermions at  $K$  and  $K'$  possess opposite chiralities. (c) Schematic of a three-dimensional (3D), A-A stacked kagome lattice, and (d) the corresponding vertical nodal lines in the hexagonal prism BZ. (e) Schematic of an A-B-C stacking of the kagome lattice and the corresponding helical nodal lines are shown in (f) and (g) from both an isometric (f) and a top (g) perspective. In (c) and (e), the dashed lines represent the interplane hopping  $t_1$  while the in-plane kagome bonds are characterized by an hopping integral  $t_0$ . In (f), we show the rhombohedral BZ along with a hexagonal prism extended from the 2D BZ illustrated in (b). (h) Surface spectra weight of the A-B-C kagome tight-binding model. A drumhead surface state (DSS) can be identified as the flat and bright intensity within the projection of the helical nodal line to the surface BZ.

electronic states and allow the study of emergent electromagnetic responses in such systems.

Motivated by the experimental discovery of quasi-two-dimensional Dirac electronic dispersions in the vicinity of the Fermi level in the ferromagnetic kagome metal  $\text{Fe}_3\text{Sn}_2$  [13], we here examine the density functional theory (DFT) electronic structure of the system in the context of three-dimensional (3D) topological nodal lines. In the following, we use the convention of Dirac fermions referring to linearly dispersing two-dimensional bands as in topological insulator surface states [14] or the two-dimensional graphene [15] and kagome models [16]. For the case of the considered 3D material, this convention includes crossing states with linear dispersion in two dimensions and preserved degeneracy in the third dimension (nodal lines), regardless of their degeneracy. This should be contrasted with the convention associated with the four-fold degeneracy of 3D Dirac semimetals that are described by the 3D Dirac equation [17]. The two-dimensional (2D) kagome lattice is composed of corner-shared triangles [see Fig. 1(a)] and is known theoretically to host Dirac fermions at its Brillouin zone corners  $K$  and  $K'$  in the electronic spectrum as illustrated in Fig. 1(b)—analogous to the honeycomb lattice [16]. In contrast to the honeycomb lattice whose experimental realization primarily falls into  $p$ -electron materials such as graphene and other main group X-enes [18], the kagome lattice has found extensive presence in a class of transition metal intermetallic compounds termed “kagome metals”, where the kagome bands are composed by  $d$  electrons [12,13,19–24]. As these compounds crystallize in three-dimensional structures, a natural question is how the notion of the point nodes in the two-dimensional

limit can be extended to the third dimension. The subject of this study—binary ferromagnetic kagome metal  $\text{Fe}_3\text{Sn}_2$  has been experimentally identified as host of bulk quasi-two-dimensional Dirac fermions in transport and photoemission spectroscopy [13], as well as in de Haas-van Alphen quantum oscillations [25] and optical conductivity [26]. Scanning tunneling microscopy has revealed a strongly anisotropic response of the electronic structure of  $\text{Fe}_3\text{Sn}_2$  due to spin-orbit coupling [27], and more recently a large number of Weyl points are also proposed to be present in the system [28]. In view of the successful application of DFT to related topological kagome metals [20,22], a comprehensive DFT study of the electronic structure of  $\text{Fe}_3\text{Sn}_2$  is expected to address the nature of its electronic topology and offer insights into the origin of experimentally observed Dirac fermions.

In this study, we first identify two sets of ferromagnetic helical nodal lines in  $\text{Fe}_3\text{Sn}_2$  near  $K$  and  $K'$  of the hexagonal Brillouin zone in the limit of vanishing spin-orbit coupling. We also found that with the introduction of spin-orbit coupling, these nodal lines are gapped into a three-dimensional quantum anomalous Hall insulating phase with out-of-plane ferromagnetic moments while with in-plane moments, point Weyl nodes remain gapless along the helices. The helical nodal lines are found to originate from the rhombohedral stacking of the bilayer kagome lattices and also subject to a layer splitting between upper and lower branches. We propose that these ferromagnetic helical nodal lines are the key to describe the observed topological electronic structure in  $\text{Fe}_3\text{Sn}_2$  and insights obtained herein can be broadly applied to various three-dimensional constructions of two-dimensional lattice models.

## II. FERROMAGNETIC HELICAL NODAL LINE IN $\text{Fe}_3\text{Sn}_2$

We start from the two-dimensional nearest neighbor tight-binding model of the kagome lattice as shown in Fig. 1(a), where we highlight the Dirac fermions located at  $K$  and  $K'$ , with opposite chirality shown in red and blue, respectively in Fig. 1(b). In Figs. 1(c)–1(g) we illustrate the effects of three-dimensional stacking with a moderate interplane hopping on these Dirac fermions. For clarity, in Figs. 1(c) and 1(e), we introduce only the in-plane nearest neighbor hopping  $t_0$  (solid lines) and the nearest out-of-plane hopping  $t_1$  (dashed lines). The location of band crossing points in the 3D Brillouin zone (BZ) with  $t_0 = 1, t_1 = 0.1$  are shown in Figs. 1(d), 1(f), and 1(g). In the simpler A-A stacking, the hopping along the  $z$  direction extends the Dirac points at  $K$  and  $K'$  to vertical nodal lines along the  $K$ - $H$  ( $K'$ - $H'$ ) directions [Fig. 1(d)]. A-B-C stacking instead results in helical nodal lines where at each  $k_z$  plane the Dirac points are shifted away from  $K$  and  $K'$  [Figs. 1(f) and 1(g)]. Here we show the BZ of the rhombohedral unit cell of the A-B-C stacking in Figs. 1(f) and 1(g) along with a hexagonal prism extended vertically from the original 2D hexagonal BZ; the projected helical nodal lines wind around the corresponding  $K$  and  $K'$  points of the latter. We show in Fig. 1(g) a top view of the helices, where within the projection onto the top surface, a weakly dispersive drumhead surface state (DSS) can be found in the surface spectral function using a large finite slab calculation [Fig. 1(h)], as is expected for prototypical topological nodal line semimetals [8]. We note that similar helical nodal lines have been discussed in the context of A-B-C stacked rhombohedral graphite [10,29–31]; there the associated drumhead surface states are theoretically anticipated to drive correlated magnetic and superconducting states [10,32] and have been observed in photoemission spectroscopy in multi-layer A-B-C stacked graphite flakes [33]. In the context of the kagome lattice, it is intriguing to note that the three-dimensional stacking allows access to a surface flat band and potential correlated states it entails, in addition to the in-plane destructive interference-induced flat band of bulk nature [23,34].

Having illustrated the generation of helical nodal lines in a simple A-B-C stacked kagome lattice model, in the following we turn to the DFT electronic structure of  $\text{Fe}_3\text{Sn}_2$  in the absence of spin-orbit coupling—to test the relevance of the above picture in describing the system. The crystalline structure of  $\text{Fe}_3\text{Sn}_2$  (space group No.166  $R\bar{3}m$ ) is illustrated in Fig. 2(a) in the conventional hexagonal unit cell, while the rhombohedral unit cell is highlighted in gray. Each unit cell contains a bilayer kagome structure that are further stacked in the A-B-C fashion. In Fig. 2(b), we show the rhombohedral BZ of  $\text{Fe}_3\text{Sn}_2$  along with selected high-symmetry points. We note that in addition to  $Z, \Gamma, B, L,$  and  $F$  of the rhombohedral convention, we also include  $M$  and  $K$  of the hexagonal convention to better describe the Dirac electronic structure observed experimentally in the proximity of  $\bar{K}$  of the surface BZ [13]. The calculated electronic structure is shown in Fig. 2(c) along the high-symmetry lines highlighted in Fig. 2(b). The majority spin states (illustrated in red) feature electron pockets centered near  $\Gamma$  and a hole pocket close to  $K$ , while the minority spin states (illustrated in blue) show a double Dirac structure displaced in energy in the vicinity of

$K$ , as previously observed in angle-resolved photoemission experiments [13,28,35]. This suggests that DFT reasonably accounts for the electronic structure in  $\text{Fe}_3\text{Sn}_2$ . Hereafter we refer to the Dirac structure near  $-0.1$  eV ( $-0.4$  eV) as upper (lower) Dirac fermions, respectively.

Focusing on the upper Dirac dispersion, although we observe an apparent gap at  $K$  similar to the DFT band structure reported in Ref. [35], via searching in the proximity of  $K$ , we find the gap closing and reopening through a single point at each constant  $k_z$  cross-section [band landscapes at selected  $k_z$  planes for the upper nodal line are shown in Figs. 2(d)–2(f)]. A search near the lower Dirac dispersion yields similar results. Connecting the point nodes at each  $k_z$  plane we obtain two sets of helical nodal lines as depicted in Fig. 2(g), where the nodal line for the upper Dirac fermion is shown in red, and lower Dirac fermions in blue. Both nodal lines wind around  $K$  vertical in a helical fashion, similar to that of the simple tight-binding model as shown in Figs. 1(f) and 1(g), suggesting that the trigonal A-B-C stacking plays a key role in generating the helical nodal lines. A magnified view of the top projection of the helical nodal lines at  $K$  and  $K'$  can be found in Figs. 2(h) and 2(i) in the shape of hypotrochoids, where we use gradient scales as shown in Fig. 2(h) to sketch the evolution along  $k_z$ . Near  $K$  both nodal lines may be approximately described by the following functional form:

$$\Delta k_x + i\Delta k_y = i\lambda_1 e^{-ik_z c} + i\lambda_2 e^{2ik_z c}. \quad (1)$$

Here the band touching point is shifted to  $(\Delta k_x, \Delta k_y)$  with respect to  $K$  point at given  $k_z$ . For the upper (lower) nodal line, the parameters are  $\lambda_1^u = 0.00928$  ( $\lambda_1^l = 0.0136$ ) and  $\lambda_2^u = 0.0087$  ( $\lambda_2^l = -0.0214$ ) in units of  $\text{\AA}^{-1}$ , respectively. Here  $c$  stands for the vertical distance between the kagome bilayer units; superscripts  $u$  and  $l$  stand for upper and lower nodal lines, respectively. The  $k_z$  evolution near  $K'$  can be obtained by performing an inversion operation to that near  $K$  [Fig. 2(i)].

The presence of sinusoidal components of both  $k_z c$  and  $2k_z c$  implies the presence of both nearest layer and next nearest layer hopping terms in  $\text{Fe}_3\text{Sn}_2$  (see Ref. [36]), the latter not included in the simple nearest layer model discussed above in Figs. 1(f)–1(h). We further examine the energy evolution of both the upper and lower nodal lines in Fig. 2(j). The closer confinement of the upper nodal lines to the verticals of  $K$  and  $K'$  is accompanied by a weaker out-of-plane dispersion illustrated in Fig. 2(j): the energy variation of the upper nodal line is on the order of 1.5 meV and for the lower is on the order of 11 meV, while both are significantly weaker as compared to the in-plane Dirac bandwidth  $\sim 2$  eV. This corroborates the bulk quasi-2D nature and the absence of photon-energy dependence of the double Dirac structure observed in  $\text{Fe}_3\text{Sn}_2$  [13].

To further elucidate the nature of the identified helical nodal lines, we have computed the Berry phase  $\Phi_B = \oint_{\Gamma_B} \mathbf{A}_k \cdot d\mathbf{k}$  on loops  $\Gamma_B$  around the nodal lines where  $\mathbf{A}_k$  is the Berry connection  $\mathbf{A}_k = -i\langle u_k | \nabla_k | u_k \rangle$  [37], with  $|u_k\rangle$  denoting the wave function at  $\mathbf{k}$ . Without spin-orbit coupling, a combined inversion and effective time-reversal symmetry dictates the quantization of the Berry phase as a binary  $Z_2$  invariant that takes either 0 or  $\pi$  [8]. We have verified that both upper and lower nodal lines support a  $\pi$ -Berry phase to the path integrals

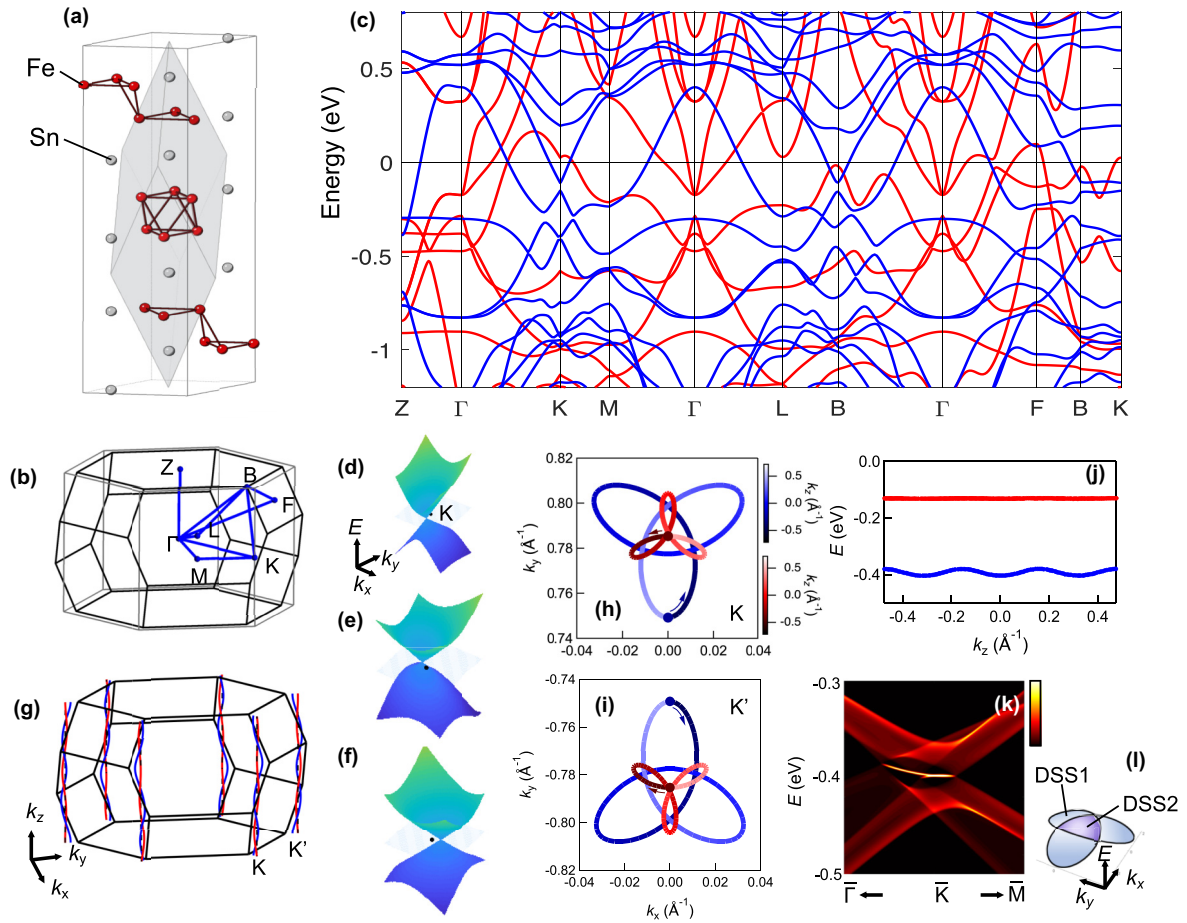


FIG. 2. Scalar-relativistic electronic structure and helical nodal lines in  $\text{Fe}_3\text{Sn}_2$ . (a) Crystal structure of  $\text{Fe}_3\text{Sn}_2$  with iron atoms shown in red and tin atoms in gray. The primitive rhombohedral unit cell containing a kagome bilayer is outlined in gray. (b) Schematic of the rhombohedral BZ of  $\text{Fe}_3\text{Sn}_2$  with high-symmetry points labeled and high-symmetry directions highlighted in blue. The gray hexagonal prism is extended from the hexagonal BZ in the 2D limit. (c) Scalar-relativistic generalized gradient approximation (GGA) DFT electronic structure of  $\text{Fe}_3\text{Sn}_2$  where the majority spin is shown in red and minority in blue. (d)-(f) DFT energy-momentum dispersion of the upper helical nodal line within a region of  $0.16 \times 0.16 \text{ \AA}^{-2}$  close to  $K$  at (d)  $k_z = 0$ , (e)  $k_z = 0.317 \text{ \AA}^{-1}$ , (f)  $k_z = -0.317 \text{ \AA}^{-1}$  planes, respectively. The black sphere denotes the  $K$  point of the 2D BZ. (g) The helical nodal lines around  $K$  and  $K'$  in  $\text{Fe}_3\text{Sn}_2$ ; the upper nodal line is shown in red and lower nodal line in blue. [(h) and (i)] Magnified top view of the helical nodal lines at  $K$  (h) and  $K'$  (i), respectively. The color gradient in (h) and (i) reflects the value of  $k_z$ . (j) Energy dispersion of both the upper and lower nodal lines along  $k_z$ . (k) Surface spectra weight of the lower nodal line inferred from the  $\mathbf{k} \cdot \mathbf{p}$  model (see Methods). (l) Schematic of two distinct momentum regions DSS1 (blue) and DSS2 (purple) that host different number of drumhead surface states. The hypotrochoid curve represents the projection of lower nodal line to the top surface.

enclosing the nodal lines, suggesting that it is the nontrivial Berry phase that protects the nodal lines in the present case. The  $\pi$ -Berry phase here may be naturally connected to that of Dirac fermions in the 2D limit [38] and that more recently demonstrated in photoemission intensity analysis for bulk quasi-2D Dirac fermions derived from the kagome lattice in  $\text{FeSn}$  [22]. In the present system, due to a reduction of the symmetry from hexagonal to trigonal, the positions of the nodal lines are displaced from high-symmetry lines; nevertheless their presence is robust and protected by the  $\pi$ -Berry phase inherited from the 2D limit. In Fig. S1 [36], we show that nodal lines centered at  $K$  and  $K'$  are robust with increasing interplane hopping strength, as long as the two lines do not touch and hybridize with each other. We note that due to broken time reversal symmetry, each band touching point here in  $\text{Fe}_3\text{Sn}_2$  is ferromagnetic and two-fold degenerate, which belongs to a similar class with the ferromagnetic nodal lines

discussed in  $\text{Co}_2\text{MnGa}$  [5],  $\text{Co}_3\text{Sn}_2\text{S}_2$  [12], and  $\text{Fe}_3\text{GeTe}_2$  [45] in the absence of spin-orbit coupling.

Additionally, we examine the surface states which originate from the hypotrochoid winding pattern of the lower nodal line in Figs. 2(k) and 2(l) (see Methods). The existence of a drumhead surface state in a nodal line semimetal may be illustrated in the following picture: for a given  $(k_x, k_y)$  one may define a Zak phase  $\Phi_Z = \int_{-\pi/c}^{\pi/c} \mathbf{A} \cdot d\mathbf{k}_z$  along  $k_z$ , and  $\Phi_Z(k_x, k_y) = \pi$  corresponds to a 1D topological insulator with zero energy edge states (here we restrict ourselves in the spinless case) and defines the  $(k_x, k_y)$  region where surface states reside [3]. In Fig. 2(k), we find that in the present case ferromagnetic drumhead surface states appear once within the three side lobes [blue region labeled DSS1 in Fig. 2(l)] with  $\Phi_Z(k_x, k_y) = \pi$  and twice within the center surface momentum regime [purple region labeled DSS2 in

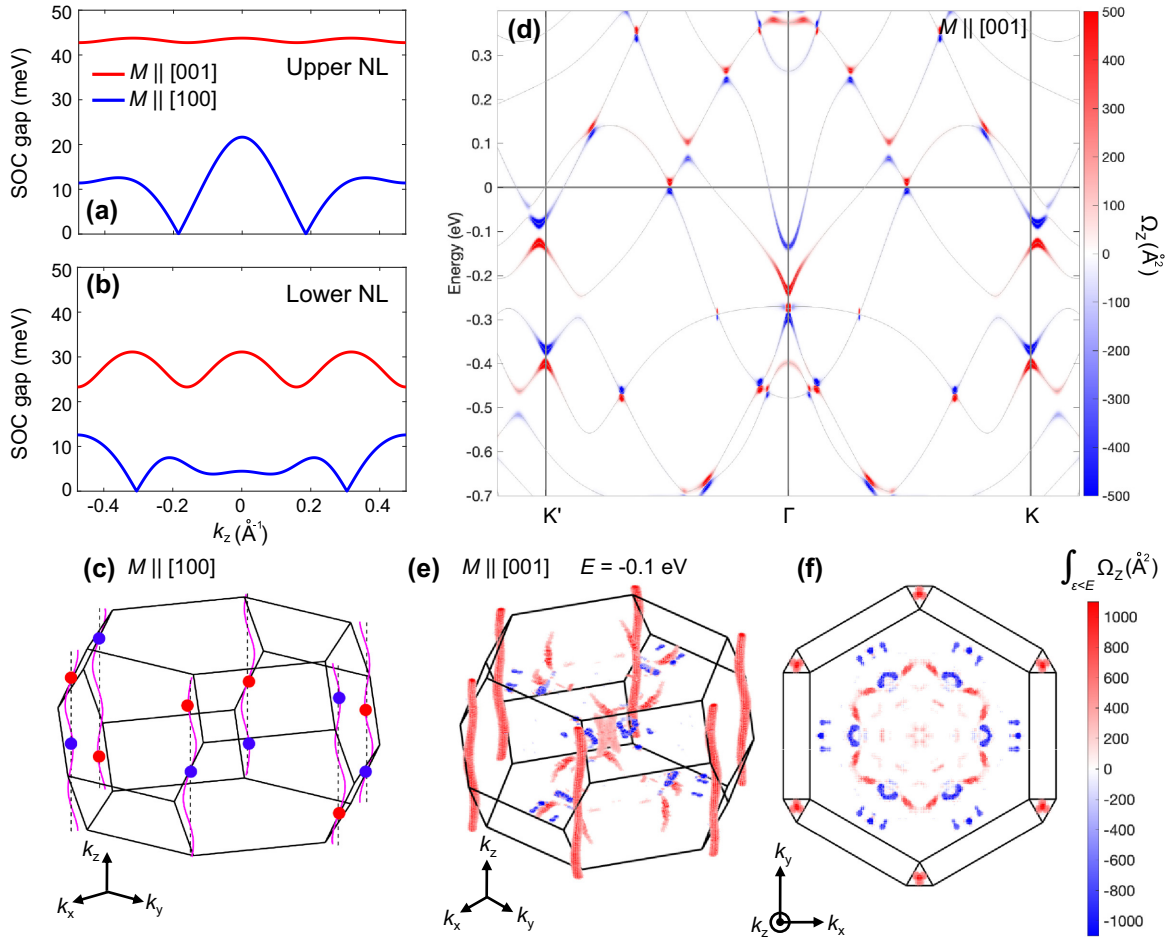


FIG. 3. Electronic structure of  $\text{Fe}_3\text{Sn}_2$  with spin-orbit coupling. (a) The gap along the helical nodal line at each  $k_z$  with ferromagnetic moment out-of-plane (red) and in-plane along [100] (blue) for the upper nodal line. (b) A similar analysis for the lower nodal line. (c) Weyl points originated from the lower helical nodal line with magnetic moment along [100]. The nodal line itself is shown in magenta. (d) The Berry curvature  $\Omega_z$  distribution with the ferromagnetic moments pointing out-of-plane along  $K'-\Gamma-K$  high-symmetry line in the band structure. (e), (f) Distribution of integrated Berry curvature (see text) up to the upper Dirac gap in the 3D BZ at  $E = -0.1$  eV in a 3D view (e) and top view (f), respectively.

Fig. 2(l)]  $\Phi_Z(k_x, k_y) = 2\pi(0)$ . We expect the surface states in the DSS2 region to be more fragile and dependent on the surface potential than that within DSS1, as has been discussed for systems with multiple nodal loops [39]. The lobe structure of the flat surface bands adds new opportunities for potential correlated phenomena; moreover, with the sensitivity of the helical nodal line to interplane hopping, one may manipulate the connectivity and drive Lifshitz transitions of these lobewise drumhead surface states by hydrostatic, uniaxial pressure, or alternatively epitaxial strain (see Fig. S12 [36]).

### III. KANE-MELE SPIN-ORBIT COUPLING IN $\text{Fe}_3\text{Sn}_2$

Having located the helical nodal lines in the proximity of  $K$  and  $K'$  in the absence of spin-orbit coupling, in the following we examine the fully relativistic electronic structure of  $\text{Fe}_3\text{Sn}_2$ . As  $\text{Fe}_3\text{Sn}_2$  is known to be a soft ferromagnet [40,41], we consider both cases of moments in and out of the kagome lattice plane. With an out-of-plane magnetic moment, we find that both the upper and lower nodal lines are fully gapped

with spin-orbit coupling, with the upper ( $43.3 \pm 0.5$ ) meV and lower Dirac gap ( $27 \pm 4$ ) meV as shown in Figs. 3(a) and 3(b). The in-plane magnetic moment induces a smaller gap, and the nodal lines remain gapless at two  $k_z$  positions for both the upper and lower branches [Figs. 3(a) and 3(b)]. This anisotropic coupling of  $\mathbf{M}$  with the Dirac electrons is consistent with a Kane-Mele type spin-orbit coupling in  $\text{Fe}_3\text{Sn}_2$  as suggested in Refs. [13,25]. These discrete remnant touching points correspond to Weyl points; we show Weyl points with the opposite chirality as blue and red circles in Fig. 3(c) for the case of the lower nodal line.

Next we elaborate on the out-of-plane ferromagnetic case where spin-orbit coupling introduces a full gap to the helical nodal lines. We have computed the resultant Berry curvature  $\boldsymbol{\Omega} = \nabla \times \mathbf{A}_k$  and its distribution along high-symmetry lines  $K'-\Gamma-K$  in  $k_z = 0$  plane is shown in Fig. 3(d). We observe concentrated Berry curvature  $\Omega_z$  at the gapped nodes as expected for massive Dirac fermions [42], together with additional distribution of Berry curvatures from potential Weyl points (see also Fig. S10 [36]) [28].  $\Omega_z$  near  $K$  and  $K'$  are found to be additive, which can be contrasted to the canceling  $\Omega_z$  pattern

at  $K$  and  $K'$  valleys in the inversion-symmetry-breaking and time-reversal-symmetric graphene [42]. The Berry curvature structure at both upper and lower Dirac gaps also exhibit the same sign. We further illustrate the distribution of integrated Berry curvature  $\int_{\epsilon < E} \Omega_z^\epsilon$  (here  $\epsilon$  represents all states with energy below  $E$ ) in the 3D BZ in Figs. 3(e) and 3(f) up to the upper Dirac gap ( $E = -0.1$  eV), where columns of Berry curvature hot spots are confined along the stacked massive Dirac fermions. These massive Dirac fermions descend naturally from their 2D limit as kagome realizations of the Haldane model [43] and therefore in isolation form a 3D quantum anomalous Hall insulating phase [44]. In this context, we propose that chiral boundary modes can be detected at step edges of the kagome cleavage of  $\text{Fe}_3\text{Sn}_2$  crystals at energies within the Dirac gap, similar to those recently demonstrated in a Mn-based kagome metal  $\text{TbMn}_6\text{Sn}_6$  [24]. Near  $\Gamma$ , we also observe less extended patches of Berry curvature intensities, the 3D nature of which suggests that they may originate from underlying Weyl fermions in the system [28]. The difference in momentum-space dimensionality leads to a response dominated by the extended  $k_z$  features associated with the massive quasi-2D Dirac states [Fig. 3(e)].

Having demonstrated that nodal lines gapped by the interplay of ferromagnetic order and spin-orbit coupling in  $\text{Fe}_3\text{Sn}_2$  serve as a strong source of Berry curvature and therefore contribute significantly to the intrinsic anomalous Hall conductivity  $\sigma_{xy}$  (see Fig. S9 [36]) [13], it is instructive to compare the helical nodal lines identified here in  $\text{Fe}_3\text{Sn}_2$  with the nodal lines discussed in the van der Waals ferromagnet  $\text{Fe}_3\text{GeTe}_2$  [45]. In both cases, topological nodal lines are rendered strong sources of  $\Omega_z$ . We note that as compared with  $\text{Fe}_3\text{GeTe}_2$ , where contribution to  $\sigma_{xy}$  is concentrated in the momentum space near the gapped nodal line along  $K$ - $H$  over its energy dispersion of 0.25 eV [45], such contributions in  $\text{Fe}_3\text{Sn}_2$  is further concentrated energetically due to the weak energy variation of the massive Dirac fermions along the  $z$  direction. Intriguingly, in  $\text{Fe}_3\text{GeTe}_2$ , it is also found that an out-of-plane moment maximizes the spin-orbit gap along the nodal line. Despite this similar sensitivity with the ferromagnetic moment orientation, we note that the spin-orbit coupling in  $\text{Fe}_3\text{Sn}_2$  that opens the gaps at the Dirac nodes is different at the effective model level than that discussed for  $\text{Fe}_3\text{GeTe}_2$  [45]. In the latter, an on-site spin-orbit coupling of the  $\mathbf{L} \cdot \mathbf{S}$  form lifts the degeneracy at  $K$  that originates from orbital degrees of freedom of Fe  $d$  orbitals; this mechanism also applies to the  $p_x, p_y$  models on the triangular lattices [46] and the  $d$  orbitals on hexagonal closed packing cobalt layers [47], where an orbital degree of freedom is preserved for three(or six)-fold rotation centers. In the context of the kagome lattice, the degeneracies of all  $d$  orbitals are in principle lifted due to the low site symmetry. An onsite spin-orbit coupling term is therefore ineffective in opening a gap for the band crossing at the effective model level, rather the intersite form of spin-orbit coupling—introduced by Kane-Mele for the graphene lattice model based on  $p_z$  orbitals [48], where the orbital degrees of freedom is quenched—is responsible for the gap opening at  $K$ . The kagome lattice therefore provides a model platform for studying the Kane-Mele type spin-orbit coupling and its interplay with massive Dirac fermions. Clarifying the underlying microscopic mechanisms for such spin-orbit coupling terms

will provide insights in future design of topological phases from the lattice point of view.

#### IV. INTERPLANE HOPPING AND LAYER DEGREES OF FREEDOM OF DIRAC FERMIONS IN $\text{Fe}_3\text{Sn}_2$

Having demonstrated that both upper and lower helical nodal lines in  $\text{Fe}_3\text{Sn}_2$  can be captured by quasi-2D Dirac fermions subject to a Kane-Mele type spin-orbit coupling, in the following we examine the origin of the pair of Dirac fermions in the system. Expanding from the A-B-C stacked kagome model described above, we build a tight-binding model of an AA-BB-CC stacked kagome lattice illustrated in Fig. 4(a) to more accurately capture the iron sublattice of  $\text{Fe}_3\text{Sn}_2$ . A fundamental rhombohedral unit cell of this model includes six atoms, forming a pair of A-A stacked kagome bilayer. This pair provides a layer degree of freedom whose role we elucidate hereafter. Aside from the in-plane nearest neighbor hopping  $t_0$ , we introduce two inequivalent interplane hopping integrals  $t_{aa}$  and  $t_{ab}$ . Here,  $t_{aa}$  represents vertical hopping processes between aligned A-A (B-B, C-C) stacked sublattices, while  $t_{ab}$  denotes the nearest neighbor hopping between layers that are rotated by  $60^\circ$  with each other (i.e., through A-B, B-C and C-A stacking).

First we find that parameter sets satisfying  $t_{ab} < t_{aa} \ll t_0$  reproduces the experimental and numerical double Dirac structure in  $\text{Fe}_3\text{Sn}_2$ : bands obtained from several such  $t_{aa}$  and  $t_{ab}$  are shown in Figs. 4(b)–4(e) and the corresponding nodal lines are shown as insets. The momentum line is highlighted in Fig. 4(b) inset. We note that setting  $t_{ab} > t_{aa}$  considerably deforms the Dirac bands (Fig. S4 [36]) and yields band features inconsistent with either ARPES [13] or the DFT spectrum shown in Fig. 2(c). Hereon we focus on the evolution of the double Dirac structure with respect to  $t_{aa}$  and  $t_{ab}$ . In Figs. 4(b), 4(d), and 4(e), a progressively increasing  $t_{ab}$  displaces the nodal lines farther from  $K$ , consistent with the simpler A-B-C model (see Fig. S1 [36]); meanwhile the energy splitting between upper and lower nodal lines stays constant. In contrast, by varying  $t_{aa}$  while keeping  $t_{ab}$  constant [Figs. 4(b) and 4(c)], the location of the nodal lines are unchanged while the energy splitting between upper and lower branches increases in proportion to  $t_{aa}$ . The respective dependence on  $t_{aa}$  and  $t_{ab}$  of the energy splitting  $\Delta E$  and momentum displacement  $\Delta k$  [both schematically illustrated in Fig. 4(e)] is also clear in the contour plots of  $\Delta E$  and  $\Delta k$  in the  $t_{aa} - t_{ab}$  phase space [Figs. 4(f) and 4(g)]. Further analysis of the eigenstates of the tight-binding Dirac states reveals that the upper/lower branches are predominately composed of bonding/antibonding superpositions of states residing respectively in layers  $L^+$  and  $L^-$  in Fig. 4(a), which are connected via  $t_{aa}$ , reminiscent of the layer splitting of Dirac states in AA-stacked bilayer graphene [49].

An outstanding observation here is that  $t_{aa}$  and  $t_{ab}$  appear to play distinct roles to the Dirac fermions. It is instructive to adopt the following  $4 \times 4 \mathbf{k} \cdot \mathbf{p}$  model in the vicinity of  $K$ :

$$\begin{aligned} \mathcal{H} = & i\hbar v_F (k_+ \sigma_- - k_- \sigma_+) + t_{aa} (e^{ik_z c_1} \tau_+ + e^{-ik_z c_1} \tau_-) \\ & + 2t_{ab} (e^{-ik_z c_2} \tau_+ \sigma_- + e^{ik_z c_2} \tau_- \sigma_+), \end{aligned} \quad (2)$$

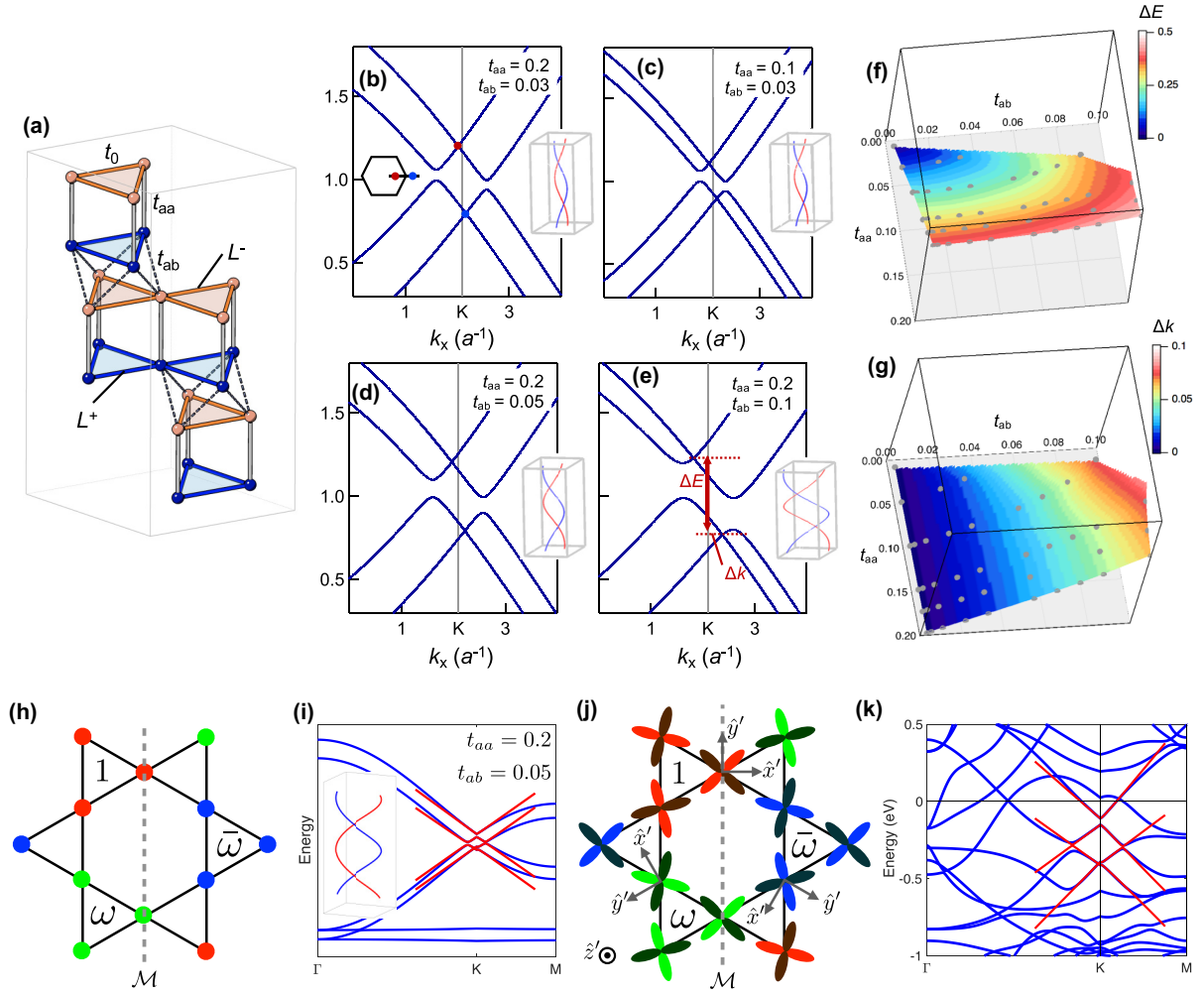


FIG. 4. Layer splitting and interplane hopping in  $\text{Fe}_3\text{Sn}_2$ . (a) Schematic of AA-BB-CC kagome lattice model with in-plane hopping  $t_0$  (dark solid bonds), interplane hopping  $t_{aa}$  (light solid bonds) and  $t_{ab}$  (dashed bonds). [(b)–(e)] Double Dirac structure near  $K$  (momentum line illustrated in (b) inset) at selected  $t_{aa}$  and  $t_{ab}$  ( $t_0 = 1$ ): (b)  $t_{aa} = 0.2$ ,  $t_{ab} = 0.03$ , (c)  $t_{aa} = 0.1$ ,  $t_{ab} = 0.03$ , (d)  $t_{aa} = 0.2$ ,  $t_{ab} = 0.05$ , and (e)  $t_{aa} = 0.2$ ,  $t_{ab} = 0.1$ . The insets show the upper (red) and lower (blue) nodal lines. Here the momentum  $k_x$  is expressed in the unit of  $a^{-1}$ , where  $a$  is the in-plane hexagonal lattice constant. [(f) and (g)] Contour plots of the energy splitting  $\Delta E$  (f) and momentum displacement  $\Delta k$  (g) in the  $t_{aa}$ - $t_{ab}$  phase space. (h) Initial wave function on a single kagome layer used to project out double Dirac structure in AA-BB-CC model. The color illustrates the phase of wavefunction: 1 (red),  $\omega = e^{i2\pi/3}$  (green) and  $\bar{\omega} = e^{-i2\pi/3}$  (blue). The other partner state is obtained by the mirror  $\mathcal{M}$  operation defined by the dashed grey line. (i) The  $\mathbf{k} \cdot \mathbf{p}$  4-band model (red) compared to the full six-band AA-BB-CC model. (j) Initial basis set of a single Fe kagome layer for  $\mathbf{k} \cdot \mathbf{p}$  projection of the double Dirac cones in  $\text{Fe}_3\text{Sn}_2$ . The rotated local coordinate frames for Fe sites are shown with the out-of-plane  $\hat{z}'$  axis. The wave function for projection is the product of the phases in (h) and the local  $d_{xy}$  orbitals. The partner state on the same layer can be obtained by mirror  $\mathcal{M}$ . (k)  $\text{Fe}_3\text{Sn}_2$  band structure (blue) compared with the projected four-band  $\mathbf{k} \cdot \mathbf{p}$  expansion (red) near  $K$  point.

where  $\sigma$  and  $\tau$  are Pauli matrices and  $v_F$  is the Dirac velocity.  $c_1$  ( $c_2$ ) represents the vertical distance of  $t_{aa}$  ( $t_{ab}$ ) hopping.  $\sigma$  represents the Dirac spinor per kagome layer [the basis wave function of  $\sigma$  within each layer is illustrated in Fig. 4(h)], while  $\tau$  denotes the layer degree of freedom where  $\tau_z |L^\pm\rangle = \pm 1 |L^\pm\rangle$ . In Fig. 4(i), we illustrate the  $\mathbf{k} \cdot \mathbf{p}$  dispersion (red) as compared with the AA-BB-CC tight-binding model (blue) for  $t_{aa} = 0.2$ ,  $t_{ab} = 0.05$ . With  $t_{ab} < t_{aa}$ , one can treat the last term of Eq. (2) as a perturbation and project the four states to two sets; the resulting two eigenstate subsectors  $D^{u,l}$  (upper ( $u$ ) and lower ( $l$ ) Dirac fermions) can be classified with  $e^{ik_z c_1} \tau_+ + e^{-ik_z c_1} \tau_- = \xi^{u,l}$  ( $\xi^u = 1$  and  $\xi^l = -1$ , respectively), which are energetically

split as  $\xi^{u,l} t_{aa}$ . Projecting the  $t_{ab}$  terms into each sector, we derive a  $2 \times 2$  effective Hamiltonian as  $\mathcal{H}_{\text{eff}}^{u,l} = i\hbar v_F (k_+ \sigma_- - k_- \sigma_+) + \xi^{u,l} t_{ab} (e^{ik_z c} \sigma_+ + e^{-ik_z c} \sigma_-) + \xi^{u,l} t_{aa}$ , where the Dirac points are moved to  $\Delta k_x + i\Delta k_y = i\xi^{u,l} \frac{t_{ab}}{v_F} e^{-ik_z c}$  ( $c = c_1 + c_2$  the vertical distance between the neighboring bilayer units), giving rise to helical nodal lines [see inset of Fig. 4(i)]. From the  $\mathbf{k} \cdot \mathbf{p}$  formulation, it is clear that  $t_{ab}$  preserves an underlying sublattice (chiral) symmetry for the Dirac fermions [50], as a result of which  $t_{ab}$  terms perturb band touching points away from  $K$  and  $K'$  but cannot generate either a gap or an energy shift to the degeneracy points. A similar  $\mathbf{k} \cdot \mathbf{p}$  model can be constructed for the DFT structure as we show in Figs. 4(j) and 4(k). The leading parameters are  $v_F = 3.8 \times 10^5$  m/s,

TABLE I. The Dirac wave function  $k_z$ -averaged ( $0 \leq k_z < 2\pi/c$ ) density distribution for Fe and Sn atomic orbitals, at the projected (2D)  $K$  point.  $\text{Sn}^{(s)}$  ( $\text{Sn}^{(k)}$ ) denotes the set of Sn atoms in spacer unit (kagome layer). The atomic orbitals are defined with the rotated local coordinate as shown in Fig. 4(j). The density is represented by the percentage projected in atomic orbitals.

	Fe $d_{xy}$	Fe $d_{x^2-y^2}$	Fe $d_{xz}$	Fe $d_{yz}$	Fe $d_{z^2}$	Fe $s$	$\text{Sn}^{(s)}$ $p_z$	$\text{Sn}^{(s)}$ $p_{x/y}$	$\text{Sn}^{(k)}$ $p$	Sn $s$
Lower Dirac cone	33.0	23.8	10.9	9.9	9.1	1.7	0.4	9.2	1.5	0.5
Upper Dirac cone	49.4	9.6	16.6	15.0	4.3	1.3	0.2	1.8	1.6	0.3

$t_{aa} = -0.13$ , eV, and  $t_{ab} = -0.0028$  eV (also see Methods), suggestive of a layer split nature of the two copies of Dirac fermions in  $\text{Fe}_3\text{Sn}_2$  [13]. The layer origin of the upper and lower Dirac states is also consistent with the similar Berry curvature structure they exhibit as illustrated in Fig. 3(d).

We additionally analyzed the orbital characters of the Wannier function for the upper and lower Dirac fermions as summarized in Table I. The predominant in-plane nature of both upper and lower Dirac fermions dictates reduced strength of  $t_{aa}$  and  $t_{ab}$  as compared to  $t_0$  (we may estimate  $t_0 \sim 0.8$  eV from  $v_F$  via  $t_0 \simeq \sqrt{3}\hbar v_F/a$ , where  $a$  is the in-plane lattice constant), which further leads to the characteristic double Dirac structure in  $\text{Fe}_3\text{Sn}_2$  (for a more detailed description of the orbital-decomposed hopping pathways see Ref. [36]). Moreover, as can be inferred from Eq. (2),  $t_{aa}$  and  $t_{ab}$  are decoupled from the  $k_z$  evolution of the nodal line energies, implying that higher order hopping terms are required to grant the Dirac fermions a considerable  $k_z$  dispersion. This is consistent with the suppressed  $k_z$  dispersion and quasi-two-dimensionality of the bulk Dirac fermions suggested experimentally in  $\text{Fe}_3\text{Sn}_2$  [13,25]. We note that including an asymmetry to account for the breathing nature of the kagome lattices in  $\text{Fe}_3\text{Sn}_2$  does not considerably alter the scenarios presented here (see Fig. S5 [36]); in particular, the inversion symmetry of the breathing distortion in the unit cell does not lift the nodal degeneracy (which is protected by a  $\pi$ -Berry phase as described above). Through the above minimal AA-BB-CC model and  $\mathbf{k} \cdot \mathbf{p}$  expansion, we establish  $\text{Fe}_3\text{Sn}_2$  as an illustrative example of how rich stacking patterns and associated interplane coupling manifest in quasi-two-dimensional electronic materials. In Fig. S6 [36], we illustrate that similar results can be obtained for a model of AA-BB-CC stacked honeycomb layers.

## V. DISCUSSION

In summary, from a band theoretical perspective, we have established  $\text{Fe}_3\text{Sn}_2$  as a host of ferromagnetic helical nodal lines derived from a kagome network of iron. The peculiar presence of mixed A-A and A-B stacking patterns of kagome lattices in  $\text{Fe}_3\text{Sn}_2$  causes the formation of helical nodal lines, gives rise to the layer splitting between upper and lower branches, and suppresses the  $k_z$ -dispersion of these nodal lines. With an out-of-plane ferromagnetic order, the two sets of helical nodal lines are gapped out by spin-orbit coupling and serve as strong source of Berry curvatures. Gradually rotating the ferromagnetic moments from out-of-plane to in-plane orientations one may partially close the Dirac mass gap at discrete points and realize pairs of Weyl nodes located along the original helical nodal lines. In view of the soft ferromagnetic nature of the system we may anticipate novel electronic states at domain walls [51]; one especially exciting avenue lies

in the skyrmion bubble structures observed earlier in  $\text{Fe}_3\text{Sn}_2$  at room temperature [52], where the real space topological spin textures may entangle with the nodal lines and give rise to novel electronic responses [53].

A direct experimental observation of the drumhead surface states in  $\text{Fe}_3\text{Sn}_2$  has remained elusive due in part to the weak interplane coupling of the  $t_{ab}$  form and a resulting limited radial size of the helical nodal lines. Aside from tuning  $\text{Fe}_3\text{Sn}_2$  utilizing hydrostatic/uniaxial pressure and epitaxial strain as we propose in this study, further engineering of the interplane hopping and spin-orbit coupling in related intermetallic compounds that host trigonal stacking of kagome lattices may lead to experimentally detectable drumhead surface states [33]. We note that a recent tight-binding study of a  $d_{z^2}$  type orbital on an A-B-C kagome lattice with enhanced out-of-plane hopping assisted by interlayer Sn atoms serves as a minimal model to generate vertical nodal rings and the ferromagnetic Weyl semimetallic phase in  $\text{Co}_3\text{Sn}_2\text{S}_2$  [54]. This comparison suggests that with rational orbital engineering, intermetallic compound-based kagome lattices may provide a full spectrum of topological phases ranging from the 3D quantum anomalous Hall insulating phase [13,22,44] to the ferromagnetic Weyl semimetallic phase [12]; driving the topological phase transition between the two classes of phases is of extreme theoretical and experimental interest.

The implications of our study are beyond electronic structures of metallic systems. As trigonal stacking and rhombohedral symmetry are ubiquitous in naturally occurring kagome lattice materials [55–58], including, for instance, the spin liquid hosting herbertsmithite [57], we expect that the helical nodal lines discussed here may be relevant not only in the electronic sector, but also in the magnonic or spinonic sectors [59], in the context of considerable inter-plane coupling. In view of the close resemblance of the kagome lattice with the honeycomb lattice [10,31,60], the above picture could be relevant, for example, in the Dirac-like Majorana fermionic spectrum in  $\alpha\text{-RuCl}_3$  where the Ru honeycomb layers are A-B-C stacked [61].

## ACKNOWLEDGMENTS

We are grateful to D. Vanderbilt, B. Lian, J.-S. You, and T. Kurumaji for fruitful discussions. This work was funded, in part, by the Gordon and Betty Moore Foundation EPiQS Initiative, Grant No. GBMF9070 to J.G.C. and NSF grant DMR-1554891. L.Y., M.K., E.K., and R.C. acknowledge support by the STC Center for Integrated Quantum Materials, NSF Grant No. DMR-1231319. L.Y. acknowledges support from the Heising-Simons Foundation. S.F. is supported by a Rutgers Center for Material Theory Distinguished Postdoctoral Fellowship. M.P.G. acknowledges the equipment grant supported

by Alexander von Humboldt Foundation, Germany. M.K. acknowledges support from Max Planck POSTECH Korea Research Initiative, the National Research Foundation of Korea, Ministry of Science and ICT (Grant No. 2016K1A4A4A01922028). J.v.d.B. acknowledges financial support from the German Research Foundation (Deutsche Forschungsgemeinschaft, DFG) via SFB1143 Project No. A5 and under German Excellence Strategy through the Wurzburg-Dresden Cluster of Excellence on Complexity and Topology in Quantum Matter ct.qmat (EXC 2147, Project No. 390858490). The computations in this paper were run on the FASRC Cannon cluster supported by the FAS Division of Science Research Computing Group at Harvard University and at the computer clusters at IFW Dresden, Germany. S.F., M.P.G. and M.R. acknowledge the technical assistance from U. Nitzsche for the latter. J.L. acknowledges the support from the Hong Kong Research Grants Council (26302118, 16305019 and N\_HKUST626/18).

## APPENDIX: METHODS

### 1. Density functional theory electronic structure calculations

To compute the electronic and related properties of  $\text{Fe}_3\text{Sn}_2$  we carry out the Density Functional Theory (DFT) calculations by using the full-potential local-orbital (FPLO) code [62], version 18.00-52. The exchange-correlation energy functional used is based on the parametrization of Perdew, Burke, and Ernzerhof (PBE-96) [63] within the generalized gradient approximation. A linear tetrahedron method with  $15 \times 15 \times 15$  subdivisions in the full Brillouin zone was used for the momentum space integrations. The lattice parameters used in the calculation are  $a = 5.3307 \text{ \AA}$  and  $c = 19.7968 \text{ \AA}$  [64]. We consider the ground state in the ferro-

magnetic state and converge the self-consistent calculations within the scalar relativistic mode, and (four-component) fully relativistic mode of FPLO, with a self-consistent spin density better than  $10^{-6}$ . The total magnetic moments per unit cell ( $\text{Fe}_6\text{Sn}_4$ ) for the converged ground states are  $12.21 \mu_B$  in scalar relativistic mode,  $12.64 \mu_B$  and  $12.65 \mu_B$  respectively for the fully relativistic mode with ferromagnetic state along [001] and [100] orientations. We note that the latter two values include orbital magnetic moments.

To carry out further analysis of the electronic structure, we derive the Wannier tight-binding Hamiltonian by projecting the Bloch states onto atomic orbital-like, maximally projected Wannier functions using the PYFPLO module of FPLO package [62,65]. These localized Wannier basis states include Fe  $4s$ ,  $3d$ , orbitals and Sn  $5s$ ,  $5p$  orbitals. The Wannier model is converged with a  $8 \times 8 \times 8$  grid sampling in the Brillouin zone. These derived Wannier Hamiltonians are then used to investigate the nodal Dirac structure and associated topological properties such as Berry curvatures [67]. The pressure modification of the helical nodal lines are simulated via DFT calculations implemented in the Vienna *ab initio* simulation package (VASP) [68,69] based on the projector augmented-wave [70] pseudopotential formalism (see Ref. [36]).

### 2. $\text{Fe}_3\text{Sn}_2$ $k \cdot p$ expansion and calculation of drumhead surface states

Here we give a more detailed  $k \cdot p$  expansion for  $\text{Fe}_3\text{Sn}_2$  electronic structure near the double Dirac cones, as performed for the AA-BB-CC model in Eq. (2). The numerical projection is based on the Wannier construction (see main text, Ref. [36] and Ref. [66]). The four-band effective Hamiltonian can be summarized as

$$\mathcal{H} = i\hbar v_F(k_+\sigma_- - k_-\sigma_+) + E_0 + (t_{aa}e^{-ik_z c_1}\tau_- + t_{ab}e^{-ik_z c_2}\tau_+\sigma_- + \text{H.c.}) + (t_1e^{-ik_z(c_1+c_2)}\sigma_- + t_2e^{-ik_z(2c_1+c_2)}\sigma_-\tau_- + t_3e^{-ik_z(c_1+2c_2)}\sigma_+\tau_+ + t_4e^{-i2k_z(c_1+c_2)}\sigma_+ + \text{H.c.}), \quad (\text{A1})$$

where  $\hbar v_F = 2.52 \text{ eV \AA}$  (corresponding to  $v_F = 3.8 \times 10^5 \text{ m/s}$ ),  $E_0 = -0.26 \text{ eV}$ ,  $t_{aa} = -0.13 \text{ eV}$ ,  $t_{ab} = -0.0028 \text{ eV}$ ,  $t_1 = 0.0123 \text{ eV}$ ,  $t_2 = 0.0059 \text{ eV}$ ,  $t_3 = -0.0339 \text{ eV}$ , and  $t_4 = -0.008 \text{ eV}$ . This effective model captures the helical nodal line structure for both upper and lower cones. Starting from this, we consider a finite thin-film slab geometry to shed light on the surface states associated with the helical nodes in  $\text{Fe}_3\text{Sn}_2$ . We found the drumhead surface states near  $K$  points as illustrated in Fig. 2(k) in the surface spectral function for the lower Dirac cone (similar drumhead surface states can be obtained for the upper Dirac cone).

- 
- [1] A. A. Burkov, M. D. Hook, and L. Balents, Topological nodal semimetals, *Phys. Rev. B* **84**, 235126 (2011).
- [2] D. Takane, S. Souma, K. Nakayama, T. Nakamura, H. Oinuma, K. Hori, K. Horiba, H. Kumigashira, N. Kimura, T. Takahashi, and T. Sato, Observation of a Dirac nodal line in  $\text{AlB}_2$ , *Phys. Rev. B* **98**, 041105(R) (2018).
- [3] Y.-H. Chan, C.-K. Chiu, M. Y. Chou, and A. P. Schnyder,  $\text{Ca}_3\text{P}_2$  and other topological semimetals with line nodes and drumhead surface states, *Phys. Rev. B* **93**, 205132 (2016).
- [4] T. Bzdušek, Q. Wu, A. Rüegg, M. Sgrist, and A. A. Soluyanov, Nodal-chain metals, *Nature (London)* **538**, 75 (2016).
- [5] G. Chang, S.-Y. Xu, X. Zhou, S.-M. Huang, B. Singh, B. Wang, I. Belopolski, J. Yin, S. Zhang, A. Bansil, H. Lin, and M. Z. Hasan, Topological Hopf and Chain link Semimetal States and Their Application to  $\text{Co}_2\text{MnGa}$ , *Phys. Rev. Lett.* **119**, 156401 (2017).
- [6] T. T. Heikkilä and G. E. Volovik, Nexus and Dirac lines in topological materials, *New J. Phys.* **17**, 093019 (2015).
- [7] Q. S. Wu, A. A. Soluyanov, and T. Bzdušek, Non-Abelian band topology in noninteracting metals, *Science* **365**, 1273 (2019).
- [8] C. Fang, H. Weng, X. Dai, and Z. Fang, Topological nodal line semimetals, *Chinese Phys. B* **25**, 117106 (2016).
- [9] S.-Y. Yang, H. Yang, E. Derunova, S. S. P. Parkin, B. Yan, and M. N. Ali, Symmetry demanded topological nodal-line materials, *Adv. Phys.: X* **3**, 1414631 (2018).
- [10] T. T. Heikkilä and G. E. Volovik, Dimensional crossover in topological matter: Evolution of the multiple Dirac point in the

- layered system to the flat band on the surface, *JETP Lett.* **93**, 59 (2011).
- [11] H. Weng, C. Fang, Z. Fang, B. A. Bernevig, and X. Dai, Weyl Semimetal Phase in Noncentrosymmetric Transition-Metal Monophosphides, *Phys. Rev. X* **5**, 011029 (2015).
- [12] E. Liu, Y. Sun, N. Kumar, L. Muechler, A. Sun, L. Jiao, S.-Y. Yang, D. Liu, A. Liang, Q. Xu, J. Kroder, V. Süß, H. Borrmann, C. Shekhar, Z. Wang, C. Xi, W. Wang, W. Schnelle, S. Wirth, Y. Chen, S. T. B. Goennenwein *et al.*, Giant anomalous Hall effect in a ferromagnetic kagome-lattice semimetal, *Nat. Phys.* **14**, 1125 (2018).
- [13] L. Ye, M. Kang, J. Liu, F. von Cube, C. R. Wicker, T. Suzuki, C. Jozwiak, A. Bostwick, E. Rotenberg, D. C. Bell, L. Fu, R. Comin, and J. G. Checkelsky, Massive Dirac fermions in a ferromagnetic kagome metal, *Nature (London)* **555**, 638 (2018).
- [14] M. Z. Hasan, and C. L. Kane, Colloquium: Topological insulators, *Rev. Mod. Phys.* **82**, 3045 (2010).
- [15] A. C. Neto, F. Guinea, N. M. Peres, K. S. Novoselov, and A. K. Geim, The electronic properties of graphene, *Rev. Mod. Phys.* **81**, 109 (2009).
- [16] R. L. Johnston and R. Hoffmann, The kagomé net: Band theoretical and topological aspects, *Polyhedron* **9**, 1901 (1990).
- [17] S. M. Young, S. Zaheer, J. C. Y. Teo, C. L. Kane, E. J. Mele, and A. M. Rappe, Dirac Semimetal in Three Dimensions, *Phys. Rev. Lett.* **108**, 140405 (2012).
- [18] S. Balendhran, S. Walia, H. Nili, S. Sriram, and M. Bhaskaran, Elemental analogues of graphene: Silicene, germanene, stanene, and phosphorene, *Small* **11**, 640 (2015).
- [19] S. Nakatsuji, N. Kiyohara, and T. Higo, Large anomalous Hall effect in a non-collinear antiferromagnet at room temperature, *Nature (London)* **527**, 212 (2015).
- [20] A. K. Nayak, J. E. Fischer, Y. Sun, B. Yan, J. Karel, A. C. Komarek, C. Shekhar, N. Kumar, W. Schnelle, J. Kübler, C. Felser, and S. S. P. Parkin, Large anomalous Hall effect driven by a nonvanishing Berry curvature in the noncollinear antiferromagnet  $Mn_3Ge$ , *Sci. Adv.* **2**, e1501870 (2016).
- [21] B. R. Ortiz, L. C. Gomes, J. R. Morey, M. Winiarski, M. Bordelon, J. S. Mangum, I. W. H. Oswald, J. A. Rodriguez-Rivera, J. R. Neilson, S. D. Wilson, E. Ertekin, T. M. McQueen, and E. S. Toberer, New kagome prototype materials: Discovery of  $KV_3Sb_5$ ,  $RbV_3Sb_5$ , and  $CsV_3Sb_5$ , *Phys. Rev. Materials* **3**, 094407 (2019).
- [22] M. Kang, L. Ye, S. Fang, J.-S. You, A. Levitan, M. Han, J. I. Facio, C. Jozwiak, A. Bostwick, E. Rotenberg, M. K. Chan, R. D. McDonald, D. Graf, K. Kaznatcheev, E. Vescovo, D. C. Bell, E. Kaxiras, J. van den Brink, M. Richter, M. P. Ghimire, J. G. Checkelsky *et al.*, Dirac fermions and flat bands in the ideal kagome metal  $FeSn$ , *Nat. Mater.* **19**, 163 (2020).
- [23] M. Kang, S. Fang, L. Ye, H. C. Po, J. Denlinger, C. Jozwiak, A. Bostwick, E. Rotenberg, E. Kaxiras, J. G. Checkelsky, and R. Comin, Topological flat bands in frustrated kagome lattice  $CoSn$ , *Nat. Commun.* **11**, 4004 (2020).
- [24] J.-X. Yin, W. Ma, T. A. Cochran, X. Xu, S. S. Zhang, H.-J. Tien, N. Shumiya, G. Cheng, K. Jiang, B. Lian, Z. Song, G. Chang, I. Belopolski, D. Multer, M. Litskevich, Z.-J. Cheng, X. P. Yang, B. Swidler, H. Zhou, H. Lin *et al.*, Quantum-limit Chern topological magnetism in  $TbMn_6Sn_6$ , *Nature (London)* **583**, 533 (2020).
- [25] L. Ye, M. K. Chan, R. D. McDonald, D. Graf, M. Kang, J. Liu, T. Suzuki, R. Comin, L. Fu, and J. G. Checkelsky, de Haas-van Alphen effect of correlated Dirac states in kagome metal  $Fe_3Sn_2$ , *Nat. Commun.* **10**, 4870 (2019).
- [26] A. Biswas, O. Iakutkina, Q. Wang, H.-C. Lei, M. Dressel, and E. Uykur, Spin-reorientation-induced band Gap in  $Fe_3Sn_2$ : Optical Signatures of Weyl Nodes, *Phys. Rev. Lett.* **125**, 076403 (2020).
- [27] J.-X. Yin, S. S. Zhang, H. Li, K. Jiang, G. Chang, B. Zhang, B. Lian, C. Xiang, I. Belopolski, H. Zheng, T. A. Cochran, S.-Y. Xu, G. Bian, K. Liu, T.-R. Chang, H. Lin, Z.-Y. Lu, Z. Wang, S. Jia, W. Wang *et al.*, Giant and anisotropic many-body spin-orbit tunability in a strongly correlated kagome magnet, *Nature (London)* **562**, 91 (2018).
- [28] M. Yao, H. Lee, N. Xu, Y. Wang, J. Ma, O. V. Yazyev, Y. Xiong, M. Shi, G. Aeppli, Y. Soh, Switchable Weyl nodes in topological kagome ferromagnet  $Fe_3Sn_2$ , [arXiv:1810.01514](https://arxiv.org/abs/1810.01514).
- [29] J. W. McClure, Electron energy band structure and electronic properties of rhombohedral graphite, *Carbon* **7**, 425 (1969).
- [30] R. Xiao, F. Tasnádi, K. Koepnick, J. W. F. Venderbos, M. Richter, and M. Taut, Density functional investigation of rhombohedral stacks of graphene: Topological surface states, nonlinear dielectric response, and bulk limit, *Phys. Rev. B* **84**, 165404 (2011).
- [31] C.-H. Ho, C.-P. Chang, and M.-F. Lin, Evolution and dimensional crossover from the bulk subbands in ABC-stacked graphene to a three-dimensional Dirac cone structure in rhombohedral graphite, *Phys. Rev. B* **93**, 075437 (2016).
- [32] M. Otani, M. Koshino, Y. Takagi, and S. Okada, Intrinsic magnetic moment on (0001) surfaces of rhombohedral graphite, *Phys. Rev. B* **81**, 161403(R) (2010).
- [33] H. Henck, J. Avila, Z. B. Aziza, D. Pierucci, J. Baima, B. Pamuk, J. Chaste, D. Utt, M. Bartos, K. Nogajewski, B. A. Piot, M. Orlita, M. Potemski, M. Calandra, M. C. Asensio, F. Mauri, C. Faugeras, and A. Ouerghi, Flat electronic bands in long sequences of rhombohedral-stacked graphene, *Phys. Rev. B* **97**, 245421 (2018).
- [34] D. L. Bergman, C. Wu, and L. Balents, Band touching from real-space topology in frustrated hopping models, *Phys. Rev. B* **78**, 125104 (2008).
- [35] H. Tanaka, Y. Fujisawa, K. Kuroda, R. Noguchi, S. Sakuragi, C. Bareille, B. Smith, C. Cacho, S. W. Jung, T. Muro, Y. Okada, and T. Kondo, Three-dimensional electronic structure in ferromagnetic  $Fe_3Sn_2$  with breathing kagome bilayers, *Phys. Rev. B* **101**, 161114(R) (2020).
- [36] See Supplemental Material at <http://link.aps.org/supplemental/10.1103/PhysRevB.105.035107> for the details of the lattice models, effective  $k \cdot p$  expansions, Wannier projections and the DFT electronic structures.
- [37] G. P. Mikitik and Y. V. Sharlai, Manifestation of Berry's Phase in Metal Physics, *Phys. Rev. Lett.* **82**, 2147 (1999).
- [38] Y. Zhang, Y.-W. Tan, H. L. Stormer, and P. Kim, Experimental observation of the quantum Hall effect and Berry's phase in graphene, *Nature (London)* **438**, 201 (2005).
- [39] Y. Zhou, F. Xiong, X. Wan, and J. An, Hopf-link topological nodal-loop semimetals, *Phys. Rev. B* **97**, 155140 (2018).
- [40] B. Malaman, D. Fruchart, and G. Le Caer, Magnetic properties of  $Fe_3Sn_2$ . II. Neutron diffraction study (and Mossbauer effect), *J. Phys. F: Met. Phys.* **8**, 2389 (1978).
- [41] R. L. Dally, D. Phelan, N. Bishop, N. J. Ghimire, and J. W. Lynn, Isotropic nature of the metallic kagome ferromagnet  $Fe_3Sn_2$  at high temperatures, *Crystals* **11**, 307 (2021).

- [42] D. Xiao, W. Yao, and Q. Niu, Valley-Contrasting Physics in Graphene: Magnetic Moment and Topological transport, *Phys. Rev. Lett.* **99**, 236809 (2007).
- [43] F. D. M. Haldane, Model for a Quantum Hall Effect Without Landau Levels: Condensed-Matter Realization of the “Parity Anomaly”, *Phys. Rev. Lett.* **61**, 2015 (1988).
- [44] A. A. Burkov, and L. Balents, Weyl Semimetal in a Topological Insulator Multilayer, *Phys. Rev. Lett.* **107**, 127205 (2011).
- [45] K. Kim, J. Seo, E. Lee, K.-T. Ko, B. S. Kim, B. G. Jang, J. M. Ok, J. Lee, Y. J. Jo, W. Kang, J. H. Shim, C. Kim, H. W. Yeom, B. I. Min, B.-J. Yang, and J. S. Kim, Large anomalous Hall current induced by topological nodal lines in a ferromagnetic van der Waals semimetal, *Nat. Mater.* **17**, 794 (2018).
- [46] J. Zhang, B. Zhao, Y. Xue, T. Zhou, and Z. Yang, Coupling effect of topological states and Chern insulators in two-dimensional triangular lattices, *Phys. Rev. B* **97**, 125430 (2018).
- [47] G. H. O. Daalderop, P. J. Kelly, and M. F. H. Schuurmans, Magnetic anisotropy of a free-standing Co monolayer and of multilayers which contain Co monolayers, *Phys. Rev. B* **50**, 9989 (1994).
- [48] C. L. Kane and E. J. Mele,  $Z_2$  Topological Order and the Quantum Spin Hall Effect, *Phys. Rev. Lett.* **95**, 146802 (2005).
- [49] C. J. Tabert and E. J. Nicol, Dynamical conductivity of AA-stacked bilayer graphene, *Phys. Rev. B* **86**, 075439 (2012).
- [50] Y. Hatsugai, T. Morimoto, T. Kawarabayashi, Y. Hamamoto, and H. Aoki, Chiral symmetry and its manifestation in optical responses in graphene: Interaction and multilayers, *New J. Phys.* **15**, 035023 (2013).
- [51] Y. Araki, A. Yoshida, and K. Nomura, Universal charge and current on magnetic domain walls in Weyl semimetals, *Phys. Rev. B* **94**, 115312 (2016).
- [52] Z. Hou, W. Ren, B. Ding, G. Xu, Y. Wang, B. Yang, Q. Zhang, Y. Zhang, E. Liu, F. Xu, W. Wang, G. Wu, X. Zhang, B. Shen, and Z. Zhang, Observation of various and spontaneous magnetic skyrmionic bubbles at room temperature in a frustrated kagome magnet with uniaxial magnetic anisotropy, *Adv. Mater.* **2017**, 1701144 (2017).
- [53] J. L. Lado and J. Fernández-Rossier, Quantum anomalous Hall effect in graphene coupled to skyrmions, *Phys. Rev. B* **92**, 115433 (2015).
- [54] A. Ozawa, and K. Nomura, Two-orbital effective model for magnetic Weyl semimetal in kagome-lattice Shandite, *J. Phys. Soc. Jpn.* **88**, 123703 (2019).
- [55] G. Xu, B. Lian, and S.-C. Zhang, Intrinsic Quantum Anomalous Hall Effect in the Kagome Lattice  $\text{Cs}_2\text{LiMn}_3\text{F}_{12}$ , *Phys. Rev. Lett.* **115**, 186802 (2015).
- [56] I. I. Mazin, H. O. Jeschke, F. Lechermann, H. Lee, M. Fink, R. Thomale, and R. Valentí, Theoretical prediction of a strongly correlated Dirac metal, *Nat. Commun.* **5**, 4261 (2014).
- [57] M. R. Norman, Colloquium: Herbertsmithite and the search for the quantum spin liquid, *Rev. Mod. Phys.* **88**, 041002 (2016).
- [58] N. Hänni, M. Frontzek, J. Hauser, D. Cheptiakov, and K. Krämer, Low temperature phases of  $\text{Na}_2\text{Ti}_3\text{Cl}_8$  revisited, *Z. Anorg. Allg. Chem.* **2017**, 2063 (2017).
- [59] Y. Ran, M. Hermele, P. A. Lee, and X.-G. Wen, Projected-Wave-Function Study of the Spin-1/2 Heisenberg Model on the Kagomé Lattice, *Phys. Rev. Lett.* **98**, 117205 (2007).
- [60] S. S. Pershoguba, S. Banerjee, J. C. Lashley, J. Park, H. Ågren, G. Aepli, and A. V. Balatsky, Dirac Magnons in Honeycomb Ferromagnets, *Phys. Rev. X* **8**, 011010 (2018).
- [61] A. Banerjee, C. A. Bridges, J.-Q. Yan, A. A. Aczel, L. Li, M. B. Stone, G. E. Granroth, M. D. Lumsden, Y. Yiu, J. Knolle, S. Bhattacharjee, D. L. Kovrizhin, R. Moessner, D. A. Tennant, D. G. Mandrus, and S. E. Nagler, Proximate Kitaev quantum spin liquid behaviour in a honeycomb magnet, *Nat. Mater.* **15**, 733 (2016).
- [62] K. Koepernik and H. Eschrig, Full-potential nonorthogonal local-orbital minimum-basis band-structure scheme, *Phys. Rev. B* **59**, 1743 (1999).
- [63] J. P. Perdew, K. Burke, and M. Ernzerhof, Generalized Gradient Approximation Made Simple, *Phys. Rev. Lett.* **77**, 3865 (1996).
- [64] K. Persson, Materials Data on  $\text{Fe}_3\text{Sn}_2$  (SG:166) by Materials Project, United States (2016), <http://doi.org/10.17188/1201722>.
- [65] <https://www.fplo.de/>.
- [66] N. Marzari, A. A. Mostofi, J. R. Yates, I. Souza, and D. Vanderbilt, Maximally localized Wannier functions: Theory and applications, *Rev. Mod. Phys.* **84**, 1419 (2012).
- [67] T. Fukui, Y. Hatsugai, and H. Suzuki, Chern numbers in discretized Brillouin zone: Efficient method of computing (spin) Hall conductances, *J. Phys. Soc. Jpn.* **74**, 1674 (2005).
- [68] G. Kresse and J. Furthmüller, Efficient iterative schemes for ab initio total-energy calculations using a plane-wave basis set, *Phys. Rev. B* **54**, 11169 (1996).
- [69] G. Kresse and J. Furthmüller, Efficiency of ab-initio total energy calculations for metals and semiconductors using a plane-wave basis set, *Comput. Mater. Sci.* **6**, 15 (1996).
- [70] P. E. Blöchl, Projector augmented-wave method, *Phys. Rev. B* **50**, 17953 (1994).